THE JOURNAL OF
PHYSICAL
CHEMISTRY C
A JOURNAL OF THE AMERICAN CHEMICAL SOCIETY

# Structural, Microstructural, and Magnetic Properties of Ce and Sr-*co*-Substituted $(La_{2-x}Vac_x)NiTiO_6$ ($x$ = 0, 0.1) Perovskites

M. Teresa Azcondo,* Mercedes Yuste, Alejandro Gómez-Pérez, Clemens Ritter, Álvaro Muñoz Noval, Julio Romero de Paz, Khalid Boulahya, Flaviano García-Alvarado, and Ulises Amador*

Cite This: *J. Phys. Chem. C* 2025, 129, 21183−21196 Read Online

ACCESS | Metrics & More | Article Recommendations | Supporting Information

**ABSTRACT:** The synthesis of materials in the $La_{2-x}(CeSr)_mSr_n\square_pNiTiO_{6-\delta}$ series (where $\square$ denotes vacancies, with $m$, $n$, and $p$ ranging from 0 to 0.2, and $x = 2m + n + p$ taking values of 0.4 and 0.6) was attempted using a modified Pechini method. A comprehensive chemical, structural, and microstructural characterization was carried out using X-ray diffraction (conventional and synchrotron), neutron powder diffraction, selected area electron diffraction, high-resolution transmission electron microscopy, and X-ray absorption spectroscopy. The results highlight that single-phase samples are obtained for compositions with low cerium and low vacancy contents ($m \leq 0.1$ and $p \leq 0.1$). The structural study reveals that the compounds present monoclinic symmetry, space groups $P2_1/n$ or $P2_1$, with Ni and Ti cations exhibiting different degrees of disorder or short-range order, influenced by the existence of A-site vacancies and the contents of $Ce^{4+}$ and $Sr^{2+}$ ions. The magnetic behavior is closely related to the cationic disorder at the B-site. The presence of antisite defects and short-range Ni−O−Ni interactions contribute to a lack of three-dimensional antiferromagnetic ordering, probably forming instead of random $Ni^{2+}$ antiferromagnetic clusters at low temperatures.

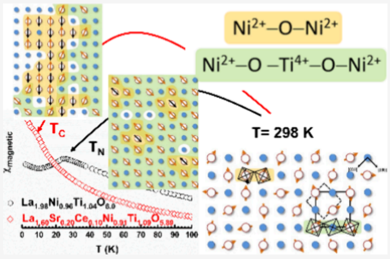

## ■ INTRODUCTION

Perovskite oxides, with general formula $ABO_3$, constitute a very versatile and easily controllable family of compounds, from both the structural and chemical points of view.[1] The structure accommodates a large variety of metal ions with varying oxidation states, and the oxide sublattice tolerates a considerable concentration of vacancies. These characteristics allow tuning of the properties of perovskite to a large extent. With respect to solid oxide fuel cell and electrolysis applications, which are among our research topics, perovskites exhibiting both mixed ionic-electronic conductivity (MIEC) and high catalytic activity are of considerable interest as electrode materials.[2−4] A simple strategy to enhance electronic conductivity is to induce mixed oxidation states in the B-site ions, while ionic-oxide conduction can be improved by creating anionic vacancies. These effects can be achieved by suitable aliovalent substitutions at the A- or B-sites of the perovskite structure.

Among the huge variety of perovskites, $LaNiO_3$-related compounds doped with various metals have attracted considerable attention as potential candidates for SOFC cathode materials due to their high electronic conductivity.[5,6] However, they exhibit low thermodynamic stability and decompose to $La_2NiO_4$ and NiO at high temperature and/or reducing conditions.[7,8] Stability can be improved by partial substitution of Ni by other less noble metals, such as Cr, Mn, Ti, and Ga.[9] Other approaches to solve stability problems are the creation of vacancies on the A-site,[10−14] the substitution of La by Ce,[15−20] and the more elaborate strategy used in the present work of codoping with Sr and Ce combined with deficiency in the A-site.

Very often, materials intended for a given application show interesting properties of a different nature; in this connection, among the materials we studied for SOFC/SOEC application, we found multiferroic compounds,[21,22] catalysts for water splitting,[23] and interesting magnetic properties.[24−28]

Thus, in the present work, we present the study of compounds derived from $La_{2-x}NiTiO_{6-\delta}$ $(0 \leq x \leq 0.2)$[27] by codoping with Sr and Ce according with the idea that $2La^{3+} \approx Ce^{4+} + Sr^{2+}$ from both the geometrical and the electrical points of view. The occupation of the perovskite A-site by up to four species ($La^{3+}$, $Sr^{2+}$, $Ce^{4+}$, and vacancies), together with the presence of two different ions in the B-sites, means that these compounds could be considered as high-entropy oxides (HEO). However, their configurational nominal entropies ($S_{config}$) are in the range (1.30−1.40) $R$ ($R$ being the ideal gas constant) that is slightly below 1.50 R, usually accepted as the lowest value for real HEOs.[29,30] However, the actual structure of materials usually results in an $S_{config}$ significantly different from the nominal ones.[31]

Received: August 18, 2025
Revised: October 1, 2025
Accepted: October 3, 2025
Published: November 18, 2025

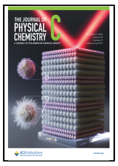

A detailed chemical, structural, and microstructural characterization, using X-ray (conventional and synchrotron), neutron powder diffraction, selected area electron diffraction, high-resolution transmission electron microscopy, and X-ray absorption spectroscopy has been performed. Finally, we performed a thorough magnetic characterization of two compounds obtained as pure phases in order to, with the previous magnetic studies carried out in the $La_{2-x}NiTiO_{6-\delta}$[27] and $La_{2-x}Sr_xNiTiO_{6-\delta}$[32] series, determine what influence the compositions in sites A and B have on the magnetic behavior of all these perovskites.

## EXPERIMENTAL SECTION

**Sample Preparation.** To favor cosubstitution of La by Ce and Sr and to ensure the homogeneity of the samples, the synthesis of materials of the $La_{2-x}(CeSr)_mSr_n\square_pNiTiO_{6-\delta}$ series (where $\square$ denotes vacancies, with $m$, $n$, and $p$ ranging from 0 to 0.2, and $x = 2m + n + p$ taking values of 0.4 and 0.6) was carried out using a modified sol−gel method. Besides, samples of compositions $La_{1.80}Sr_{0.20}NiTiO_{6-\delta}$ and $La_{1.85}NiTiO_{6-\delta}$ previously reported[27,32] were prepared for comparison. Approximately 10 g of each composition was prepared by dissolving stoichiometric amounts of high-purity Ni (Aldrich 99.99%), $La_2O_3$ (Alfa Aesar, 99.9%), $SrCO_3$ Aldrich 99.9%), and $Ce(NO_3)_4$ (99.9% Aldrich) in ca. 20 mL of hot nitric acid (Panreac 66%), before adding 50 mL of distilled water. Citric acid was subsequently added in a 3:1 molar ratio of citric acid:metal ions under conditions of constant heating and vigorous stirring. This citric acid-to-metal ion ratio favors homogeneous distribution of metals through the solution by the formation of chelate-complexes $Metal(Acetate)_3$. Since there are very few nonhydrolyzable water-soluble salts of titanium,[33] finely divided insoluble $TiO_2$ powder (anatase, Aldrich 99.9%) was then added, obtaining a homogeneous suspension. Once the volume had reduced by half, 3 mL of diethylene glycol was added to promote polymerization. The resulting solid resin was cooled to room temperature and milled in an agate mortar, and the powder was burnt at 1073 K to remove the organic matter. After milling and homogenization, the resulting powder was fired at 1773 K for 24 h, cooling down to room temperature at $\approx 2\ K\ min^{-1}$.

**Characterization Techniques.** Sample purity was determined by powder X-ray diffraction (XRD) on a Bruker D8 high-resolution diffractometer equipped with a solid-state position sensitive rapid LynxEye detector (PSD) using monochromatic $CuK_{\lambda 1}$ ($\lambda$ = 1.5406 Å) radiation obtained with a germanium primary monochromator. The angular range, step size, and counting times were selected to ensure the required data quality and resolution for structural refinement.

The chemical composition of the samples was determined by electron-dispersive spectroscopy (EDS) using an EDAX detector on an FEI XL30 scanning microscope by analyzing about 20 grains of every sample.

Synchrotron radiation high-resolution powder X-ray diffraction (SR-HRPD) patterns were collected on the SpLine Spanish CRG beamline BM25A at the European Synchrotron Radiation Facility (ESRF), Grenoble (France). The monochromator is a pseudochannel cut with two fixed Si(111) crystals moved together by a simple goniometer circle, in the $(-n,+n)$ configuration. The first monochromator crystal is ethanol-cooled, while the second crystal is kept at room temperature. The second crystal is equipped with a piezoelectric driver that allows very slight changes in the Bragg angle (pitch adjustment) in order to reduce the harmonic content of the beam, if necessary, and to keep the transmission of the monochromator constant during long-time intervals. Also, a bender curves sagittally the second crystal in order to focus the beam at the sample position.[34] The sample was finely ground and loaded into a 0.4 mm diameter borosilicate capillary mounted on a spinning goniometer. Room-temperature data were collected in a continuous $2\theta$-scan mode from 7° to 48° using an incident wavelength of 0.62100(6) Å (calibrated with NIST SRM 640c silicon powder; $a$ = 5.431195(9) Å). The counts from the different channels were rebinned to produce an equivalent normalized step scan of 0.01 step intervals, with a count time of 1 s per step.

Neutron powder diffraction (NPD) experiments at room temperature were performed on two different apparatuses at the Institute Laue-Langevin: on the high-resolution diffractometer D2B, a monochromatic beam of wavelength 1.5940 Å was selected with a Ge monochromator from the primary beam, the divergence of which was defined by an additional 10′ collimator to increase the instrumental resolution whereas on D1B, a monochromatic beam of 1.2902 A was used. The instrumental contribution to line broadening and the precise determination of wavelengths were evaluated using NIST standard samples of $Na_2Ca_3Al_2F_{14}$ and Si, respectively. Structural refinements were carried out by the Rietveld method using the FullProf program[35] by joint fitting of SR-HRPD and NPD data. The neutron scattering amplitudes used in the refinement were 0.824, 0.7020, 0.4840, 1.03, −0.344, and 0.581 ($10^{-12}$cm) for La, Sr, Ce, Ni, Ti, and O, respectively; isotropic thermal factors (ITF) were used for all atoms. Constraints employed throughout refinement involved considering the perovskite B-sites fully occupied and adopting the same thermal factor for all oxygen atoms.

The nickel oxidation state and oxygen content (assuming charge neutrality) of samples were determined by titration using potassium dichromate, as described in ref 28. Independent determinations were performed by thermogravimetric analyses using a D200 Cahn Balance. Typically, ca. 70 mg of the sample was weighed to a precision of ± 0.0005 mg at a total reduced pressure of 400 mbar containing 60% He and 40% $H_2$. The sample was then heated to 1173 at a rate of $5\ K\ min^{-1}$.

X-ray absorption spectroscopy experiments were carried out at the Ti and Ni K-edges (4966 and 8333 eV, respectively) at the absorption experimental station in BM25A, the Spanish CRG at ESRF. This station is equipped with a double Si(111) crystal monochromator of pseudo channel-cut type refrigerated at 200 K by a homemade ethanol cooling system. The setup allows the performance of experiments in transmission and fluorescence yield modes. The fluorescence signal is registered in a Si(Li) 13-elements detector (SGX Sensortech). Ni reference spectra were acquired in transmission mode, and all the samples were mounted in pellets in a controlled mixture of KBr, whose concentrations were calculated to optimize the XAS signal. At least three spectra were acquired for each sample and condition to increase the signal-to-noise ratio. Extended X-ray absorption fine structure (EXAFS) spectra were acquired upon photoelectron wavenumber values of 15 $Å^{-1}$ for Ni and 10 $Å^{-1}$ for the Ti K-edges, respectively. The Demeter software[36] was employed in the EXAFS data reduction and the fits performed in both $r$ and $k$ spaces in the range $\Delta R$ = 1−3 Å and $\Delta k$ = 1.8−12 $Å^{-1}$ for Ni and $\Delta R$ = 1−3 Å and $\Delta k$ = 3−8 $Å^{-1}$ for Ti. The scattering paths employed for fits were calculated using FEFF8.4[37] with crystallographic structures of NiO to obtain the scattering paths corresponding to the first O shell in the octahedral coordination.[38] To reduce the parameter correlations, they have

**Table 1. Results of the Syntheses of Samples with Nominal Composition Given as $La_{2-x}(CeSr)_mSr_n\square_pNiTiO_{6-\delta}$, where $\square$ denotes A-site vacancies and the maximum value of anion vacancies; $\delta$ is given as $\delta = 1/2\ (n + 3p)$ assuming no $Ni^{3+}$ in the compound[a]**

| ID code | $m$ | $n$ | $p$ | max $\delta$ | Comments | chemical composition |
|---|---|---|---|---|---|---|
| LCSNT102000 | 0.10 | 0.20 | 0.00 | 0.10 | Single-phase, 2% NiO | La1.60(1)Ce0.10(2)Sr0.30(2)Ni0.98(2)Ti1.02(2)O6.00(4) |
| LCSNT101010 | 0.10 | 0.10 | 0.10 | 0.20 | Single-phase, 2% NiO | La1.60(1)Ce0.10(1)Sr0.20(1)Ni0.91(2)Ti1.09(2)O5.89(4) |
| LCSNT200020 | 0.20 | 0.00 | 0.20 | 0.30 | $CeO_2$ and NiO segregate | |
| LCSNT200030 | 0.20 | 0.00 | 0.30 | 0.45 | Complex mixture | |
| LCSNT002000 | 0.00 | 0.20 | 0.00 | 0.10 | Single-phase, 3% NiO | [b]La1.80(1)Sr0.20(1)Ni0.92(2)Ti1.08(2)O5.92(4) |
| LCSNT000015 | 0.00 | 0.00 | 0.15 | 0.30 | Single-phase, 3% NiO | [c]La1.86(3)Ni0.87(3)Ti1.13(3)O5.92(4) |

[a] Chemical composition was obtained by EDS and NPD. The generic ID code is given as LCSNTmnp, corresponding to the chemical formula $La_{2-(2m+n+p)}Ce_mSr_{m+n}\square_pNiTiO_{6-\delta}$. [b] From ref 32. [c] From ref 27.

been reduced to a minimum, using as the upper limit the Nyquist criterion ($n = 2\Delta k\Delta R/\pi$). However, as the EXAFS spectra achieved quality enough, we were able to reach $k$ values of 12 Å$^{-1}$ for Ni K-edge and therefore the number of variables was always kept to consistent values and correlations lied in negligible values.

The dependence of the magnetization ($M$) on the temperature ($T$) and the applied magnetic field (H) of the studied compounds was obtained using a superconducting quantum interference device magnetometer (Quantum Design, model MPMS-XL). The diamagnetic contribution of each sample was considered. Magnetic susceptibility ($\chi$) was calculated as $M/H$ and normalized to a content of 1 mol of nickel per formula. Measuring modes of zero-field cooling (ZFC) and field cooling (FC) were used.

## ■ RESULTS AND DISCUSSION

**Compositional Range and Sample Purity.** Table 1 summarizes the results of the syntheses of samples with different nominal compositions, whereas Figure S1 shows the XRD patterns of the single-phase samples. Within the experimental errors, those samples whose nominal compositions imply low Ce-contents ($m \leq 0.10$) and oxygen vacancy concentrations not too high ($\delta \leq 0.30$) are single-phase with actual compositions close to the nominal ones, though segregation of some NiO is observed as in similar materials.[27,32] The distribution of all the constituting elements was confirmed to be homogeneous throughout the samples; no segregated phases are observed. As an example, Figure 1 shows a BSE SEM image (a) of a sample LCSNT101010 (i.e., with nominal composition $La_{1.60}Ce_{0.10}Sr_{0.20}NiTiO_{5.80}$) together with the corresponding element-distribution maps (b)−(g) and a tomographic image (h).

Unlike what was observed in Figure 1, the corresponding SEM/EDS maps of LCSNT200020 shown in Figure S2 clearly reveal the segregation of NiO, in agreement with the results obtained by NPD (see Figure S3).

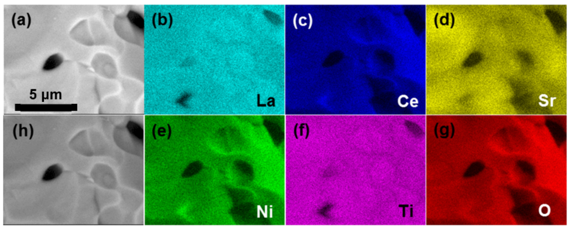

**Figure 1.** (a) Backscattered electrons (BSE) image taken at a magnification of ×4000 and the corresponding element-distribution maps of a LCSNT101010 sample. (b) La, (c) Ce, (d) Sr, (e) Ni, (f) Ti, and (g) O; (h) tomographic image revealing pores in the pellet as dark contrast.

Based on the hypothesis that $2La^{3+} \approx Ce^{4+} + Sr^{2+}$—from both a geometrical (ion sizes ($^{XII}r(La^{3+}) = 1.36$ Å, $^{XII}r(Ce^{4+}) = 1.14$ Å, $^{XII}r(Sr^{2+}) = 1.44$ Å)) and electrical point of view—the syntheses of samples with different nominal compositions were tried. We attempted to create A-site vacancies, i.e., decreasing the La + Ce + Sr: Ni + Ti ratio below 1, which corresponds to $p \neq 0$, by changing either the Ce/Sr ratio away from 1:1 ($n \neq 0$) or by keeping the Ce/Sr 1:1 ($n = 0$) ratio. In the latter case, the compositions we tried (as in LCSNT200020 and LCSNT200030) seemed to contain too many A-site vacancies and did not give single-phase products. Maybe, some intermediate compositions, such as LCSNT200010, could result in pure samples. Table 1 shows the synthesis results together with information about the previously prepared compounds: $La_{1.80}Sr_{0.20}NiTiO_{6-\delta}$ and $La_{1.85}\square_{0.15}NiTiO_{6-\delta}$. The latter corresponds to the limit of A-site vacancies the parent oxide $La_2NiTiO_6$ can tolerate whereas the former corresponds to an intermediate composition in the $La_{2-x}Sr_xNiTiO_{6-\delta}$ series.

A sample combining A-site vacancies and La substitution according to the general scheme $2La^{3+} = Ce^{4+} + Sr^{2+}$ was prepared for $m = 0.1$ and $p = 0.1$ (LCSNT101010). It could be thought that in the $La_{2-x}(CeSr)_mSr_n\square_pNiTiO_{6-\delta}$ series, similar compositional limits for aliovalent substitution and A-site vacancy concentration as in the no-containing-Ce series can be reached. In the series $La_{2-x}Sr_xNiTiO_{6-\delta}$, the upper limit for La substitution is $x \leq 0.50$, whereas in $La_{2-x}NiTiO_{6-\delta}$, the limit for A-site deficiency is $x \leq 0.20$. Thus, in the studied series, the values of $p$ would be $0 \leq p \leq 0.20$ and for $p = 0$, the value of ($2m + n$) would rise to 0.50. However, single-phase samples are obtained only for those compositions with low cerium contents, $m \leq 0.10$, in agreement with previous results.[20,39] Thus, samples LCSNT102000 and LCSNT101010 are single-phase (Figure S1) whereas LCSNT200020 samples, with nominal composition $La_{1.40}Ce_{0.20}Sr_{0.20}\square_{0.20}NiTiO_{6-\delta}$, consist of a mixture of a perovskite with actual composition far from the nominal one, NiO and $CeO_2$ (Figure S2 shows the corresponding NPD pattern). On the other hand, the sample LCSNT200030 ($La_{1.30}Ce_{0.20}Sr_{0.20}\square_{0.30}NiTiO_{6-\delta}$) is a complex mixture of a perovskite and segregated oxides.

The compositions of single-phase samples given in Table 1 were determined by combining SR-HRPD, NPD, and SEM (EDS). Even in these cases, NPD revealed the presence of some unreacted or segregated NiO, indicating off-stoichiometry. Thus, the Ti/Ni ratio is always slightly greater than the nominal one (1:1). This was observed by EDS analyses and NPD refinements as well; therefore, the actual stoichiometries exhibit Ti excess and Ni deficiency. This feature seems to be related to the number of A-site vacancies, i.e., the value of "$p$", in such a way that the difference between the nominal and actual nickel-to-titanium ratios increases with increasing nominal A-site vacancy concentration. Therefore, it seems that the structure cannot tolerate either a large amount of A-site ($p < 0.20$) or anionic vacancies ($\delta \leq 0.10$). Hence, the concentrations of A- and oxygen vacancies are significantly lower than the nominal values and besides, $Ti^{4+}$ replaces some $Ni^{2+}$ to compensate.

**Crystal Structures.** SAED and HRTEM have been used to help in the development of an appropriate structural model and to determine the existence of defects or short-range ordering effects, which are difficult to detect by average diffraction techniques such as SR-HRPD and NPD.

In the parent compound $La_2NiTiO_6$, $Ni^{2+}$ and $Ti^{4+}$ are ordered, although some degree of intermixing or antisite defects (AS) of Ni and Ti on the B′ and B″ sites, respectively, is present (ca. ∼8%). This compound was reported[32] to be slightly Ni-deficient and with a small amount of NiO. Similarly, LCSNT102000 and LCSNT101010 present some Ni sub-stoichiometry (and consequently, they are slightly Ti-over-stoichiometric, ca. ∼7% atom) as detected by NPD. This Ti overstoichiometry, accompanied by a small amount of segregated NiO, seems to be very common in nickelates.[10−12,14]

Rock-salt-like ordering of Ni and Ti exists in the $La_{2-x}Sr_xNiTiO_{6-\delta}$ series; however, the order is suppressed for $x > 0.10$.[32] SR-HRPD and NPD have been used to determine the average structure of the title compounds to be compared with the information obtained from transmission electron microscopy.

**Sample LCSNT101010.** Figure 2 shows the HRTEM images and the corresponding FT taken on two crystals of sample LCSNT101010 ($La_{1.60}Ce_{0.1}Sr_{0.20}\square_{0.10}NiTiO_{6-\delta}$) with different orientations. The crystals consist of intergrown domains with different orientations; however, the contrast differences can be associated with a unit cell $2^{1/2}a_p \times 2^{1/2}a_p \times 2a_p$. Thus, in Figure 2a, the two domains indicated as A and B display a contrast variation with periodicity ($2^{1/2}a_p \times 2a_p$) but with the $2^{1/2}a_p$-axis rotated by 90° along the $2a_p$-axis. Besides, the two diagonal perovskites axes ($2^{1/2}a_p$) are dissimilar to each other, and the cell is monoclinic as suggests the splits of the peaks at high angles (indicated by an arrow on the FFT of the crystal with an aperture encompassing domains A and B). FT diagrams of these two domains in Figure 2a are indexed using the aforementioned diagonal perovskite cell; these patterns together with those in Figure 2b suggest the extinction conditions corresponding to S.G. $P2_1/n$ ((hkl) = none, (0k0) $k = 2n$, (h0l) $h+l = 2n$); the spots in the FT along [001] on Figure 2b are due to dynamical effects since they do not appear in thin crystals.

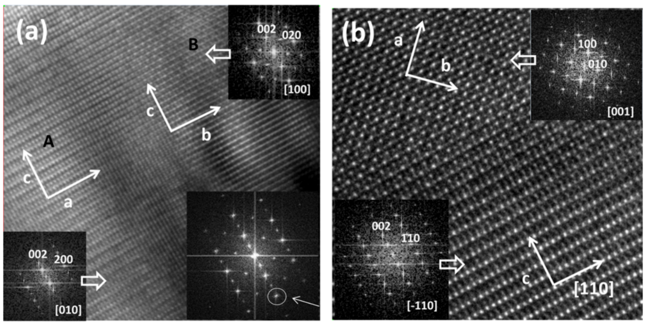

**Figure 2.** HRTEM images and the corresponding FT taken on two crystals of sample LCSNT101010 in different orientations (a,b).

Double perovskites, $A'A''B'B''O_6$, with diagonal unit cell and S.G. $P2_1/n$ (#14) present tilting of the $(B'/B'')O_6$ octahedra and rock-salt order of B′ and B″ ions, whereas A-sites are occupied at random.[1,40,41] According to these theoretical studies, the tilting scheme compatible with this S.G. is ($a^-a^-c^+$) (indicating that the octahedra rotate in opposite directions in consecutive layers along the Cartesian axes $x$ and $y$, whereas along the $z$-axis, they rotate in the same direction). If no rock-salt order exists, then the tilting scheme ($a^-a^-c^+$) results in an orthorhombic symmetry (S.G. *Pnma* #62). Thus, HREM and SAED allow proposing a detailed structural model, at least at a local scale; SR-HRPD and NPD will be used to confirm this model as representative of the average structure of this LCSNT101010 oxide. Figure 3 shows the graphic result of the fitting of NPD data to the model presented in Table S1.

On the other hand, LCSNT101010 compares to $La_{1.85}NiTiO_{6-\delta}$. In this material, Ni and Ti remain ordered, the symmetry being monoclinic as determined by SAED, as in the entire $La_{2-x}NiTiO_{6-\delta}$ series, since the rock-salt order in the B-sites is not suppressed by creation of A-sites vacancies.[32] A similar behavior is found in the analogous series containing Co.[42] In LCSNT101010, the rock-salt order of the B-sites persists not only in the presence of vacancies but also of a high number of antisite defects (around 31%) (Table S1). It is worth noting that in the NPD pattern (Figure 3), the strongest peaks related to the rock-salt order (i.e., (011), (−101), and (101)) are broad, suggesting that this order is short-range.

In some members of the A-site-deficient perovskite series $La_{2-x}NiTiO_{6-\delta}$[27] and $La_{2-x}CoTiO_{6-\delta}$,[42] additional order on the A-sites is observed. On the contrary, in LCSNT101010, no such ordering is present, most likely due to the configurational entropy associated with four species sharing the A-sites: $La^{3+}$, $Sr^{2+}$, $Ce^{4+}$, and vacancies. Indeed, the $S_{config}$ calculated for the actual structure presented in Table S1 is 1.58R, noticeably higher than the nominal one (1.40R); the difference between both values is due to two effects: the antisite defects and the existence of oxygen vacancies. The Ni oxidation state calculated assuming electroneutrality and the rest of the metals in their common oxidation states is 2.02(3). This means that a small amount of $Ni^{3+}$ may exist in this oxide, which could play an important role in its physical properties.

**Sample LCSNT102000.** Formally, LCSNT102000 (with composition $La_{1.60}Ce_{0.10}Sr_{0.30}NiTiO_{6-\delta}$) compares to $La_{1.80}Sr_{0.20}NiTiO_{6-\delta}$, in that the A-sites are fully occupied, but for this compound Ni and Ti are disordered and the symmetry is *Pnma*;[32] while LCSNT102000 presents a monoclinic symmetry. In the corresponding SR-HRPD pattern shown in Figure 4, in addition to reflections of a typical simple cubic perovskite, a set of extra peaks is observed, suggesting a superstructure with a larger cell. Those fundamental reflections are clearly split at high diffraction angles, indicating a deviation from the cubic symmetry. Particularly interesting is the splitting of the $(222)_p$ simple-cubic-perovskite peak into three, (inset to Figure 4), resulting in a triclinic distortion of the prototype cubic cell: $\mathbf{a_p}' \neq \mathbf{b_p}' \neq \mathbf{c_p}'$ and $\alpha \neq \beta \neq \gamma \neq 90°$. This triclinic cell can be transformed into a primitive monoclinic cell, whose basis vectors relate to the basis vectors of the cubic prototype cell according to $\mathbf{a_m} = 1/2\ (\mathbf{a_p} + \mathbf{b_p})$, $\mathbf{b_m} = 1/2\ (-\mathbf{a_p} + \mathbf{b_p})$, and $\mathbf{c_m} = \mathbf{c_p}$.[43]

HRTEM helps to determine the exact S.G. and the orientation of the symmetry elements within the unit cell. Figure 5 shows the HRTEM image and the corresponding FT taken on a crystal of

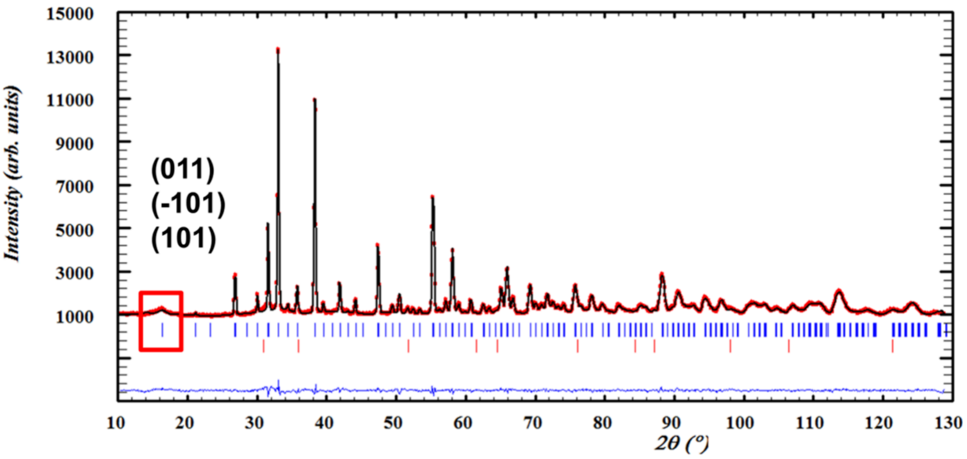

**Figure 3.** Graphic result of the fitting of NPD data of (LCSNT101010) with the model given in Table S1; experimental (red points), calculated (solid black line), and their difference (blue line at bottom) patterns are plotted. The vertical bars indicate the positions of the Bragg peaks of LCSNT101010 (upper row in blue) and NiO (lower row in red). The highlighted broad peaks are associated with short-range NaCl-like cation ordering.

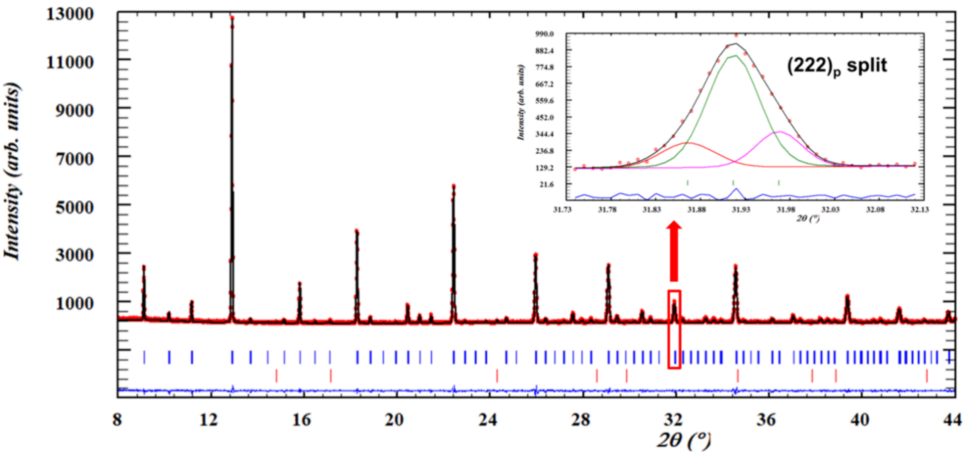

**Figure 4.** Graphic result of the LeBail fitting of SR-HRPD data for LCSNT102000 with a diagonal monoclinic cell of $2^{1/2}a_p \times 2^{1/2}a_p \times 2a_p$ and $\beta \approx 90°$ with no extinctions. The experimental (red points), calculated (solid black line), and their difference (blue line at bottom) patterns are plotted. The vertical bars indicate the positions of the Bragg peaks of LCSNT102000 (upper row in blue) and NiO (lower row in red). The inset shows the splitting of the $(222)_p$ simple-cubic perovskite, suggesting a monoclinic symmetry.

LCSNT102000. Two kinds of domains, indicated as A and B, are clearly observed. In both domains, the contrast differences show a periodicity ($2^{1/2}a_p \times 2a_p$) with the $2^{1/2}a_p$-axis rotated by 90° around the $2a_p$-axis. Again, the split of some high-angle spots (images not shown) confirms that the cell is monoclinic. The extinction conditions observed in the FT in the insets of Figure 5 point to S.G. $P2_1/n$ with a cell orientation of $2^{1/2}a_p \times 2^{1/2}a_p \times 2a_p$ and $\beta \approx 90°$.

As a structural starting model to fit the SR-HRPD and NPD patterns, we used one like that previously described for LCSNT101010 (Table S1). However, as clearly seen in Figure S4, the fitting of the SR-HRPD pattern is not good; some peaks are poorly fitted, suggesting that some structural features related to heavy atoms are not well captured in the model. Even more, since Ni and Ti have virtually the same X-ray scattering factor, that structural effect most likely is due to the arrangement of A-site metals: La/Ce and Sr. Removing the *n*-glide plane from S.G. $P2_1/n$ allows the splitting of the A-metal 4e Wickoff site into two 2a sites in S.G. $P2_1$. The final structural model for LCSNT102000 is given in Table S1, and the graphic result of the fitting of NPD data is depicted in Figure 6.

Interestingly, although in the final refined model in Table S1 Ni and Ti are distributed almost at random, the symmetry of this material is monoclinic, not only at short-range (as demonstrated by SAED) but also in the average structure. We tried to refine the NPD and SR-HRPD data using a disordered *Pnma* model, but the fitting is much worse. The reason for this lowering in symmetry from *Pnma* to $P2_1$ is not the order of B ions, accounted in S.G: $P2_1/n$,[41] but the ability of this S.G. to provide more degrees of freedom to the oxygen atoms in such a way that different local $AO_n$ environments are available in the structure to accommodate the three species hosted in the A-positions: $La^{3+}$, $Sr^{2+}$, and $Ce^{4+}$. Worth noting, the ordering of B ions is compatible with S.G. $P2_1/n$; however, when additional ordering of the A-metals occurs, the symmetry lowers. The corresponding $S_{config}$ for this model, with no oxygen vacancies (Table S1), is noticeably lower than the nominal one (1.161R for the former and 1.306R for the latter).

The perovskite LCSNT102000 presents a tilting scheme ($a^-b^-c^+$) instead of the more common ($a^-a^-c^+$) characteristic of S.G. $P2_1/n$; the inequality of the out of phase tilts creates crystallographically inequivalent A- (and B-) sites that permit ordering of the A-cations (but do not require it). In the present

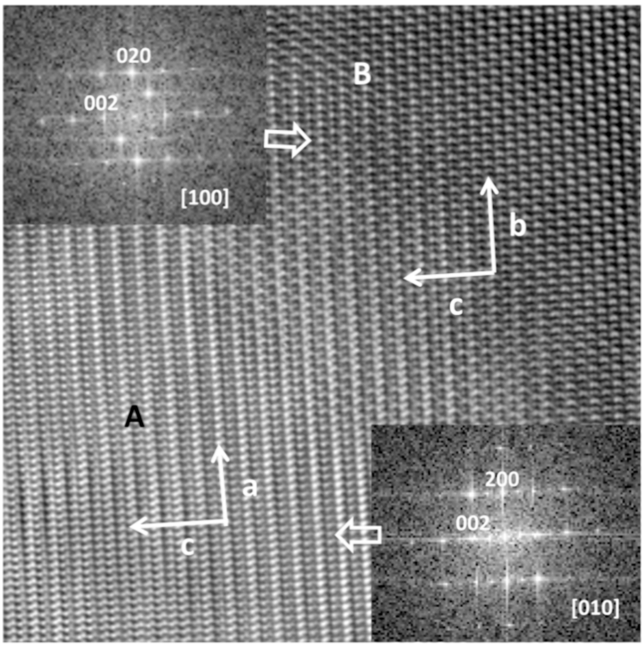

**Figure 5.** HRTEM image and the corresponding FT taken on a crystal of LCSNT102000.

case, the B-sites are almost equally populated by Ti and Ni, but the low symmetry allows laminar ordering of A-ions along the *c*-axis (Figure S5). The Jahn−Teller effect related to the electronic configuration of $Ni^{2+}$ in the octahedral configuration ($t_{2g}^6e_g^2$) may be the driving force for the symmetry lowering observed in this compound.

Finally, the oxygen substructure is fully occupied in LCSNT102000 in contrast to that observed in LCSNT101010. Besides, in the former, the Ni oxidation state is with 2.05(2) (5% of $Ni^{3+}$) higher than in the latter with 2.02(3). Thus, it seems that the aliovalent substitution $La^{3+}$ by $Sr^{2+}$ is more effective in the oxidation of Ni ions; a similar behavior has been found in the $La_{2-x}Sr_xNiTiO_{6\text{-}\delta}$ and $La_{2-x}NiTiO_{6\text{-}\delta}$ series.[27,32] Redox titration and thermogravimetric analyses suggest that the amount of $Ni^{3+}$ in LCSNT101010 and LCSNT102000 is in the range of (0.7−1.0)% (slightly higher in the latter) and very close to what is found in the *A*-site deficient perovskite $La_{1.80}NiTiO_{6\text{-}\delta}$ but lower than that of $La_{1.80}Sr_{0.20}NiTiO_{6\text{-}\delta}$. Therefore, A-site vacancies seem to promote the creation of oxygen vacancies, as observed in the reference compounds. The presence of trivalent nickel plays an important role in the physical properties of these materials.

The BVS data in Table S2 confirm some chemical and structural information about the LCSNT101010 and LCSNT102000 phases. The average oxidation states of the 3d-metals are higher in the latter phase, in agreement with the redox titration, the oxygen content in Table S1, and the $Ti^{4+}$ overstoichiometry. This results in a higher concentration of antisite defects LCSNT102000. In LCSNT101010, Ni preferentially occupies the B′ sites, while Ni and Ti are randomly distributed between the B′ and B″ sites in LCSNT102000, which is reflected in the average BVS of the two sites. Finally, to allow for the random distribution of cations, MO6 octahedra must be distorted, as reported in Table S2.

**3d-Metal Environments and Valences.** *Ni K-Edge.* Ni XAS spectra of samples LCSNT102000, LCSNT101010, LCSNT002000, LCSNT000015, and references Ni and NiO are presented in Figure 7. The variations in the white-line shape are associated with differences in the Ni local environment, including symmetry and the oxidation state. The edge position shift is a well-known indicative of the oxidation state of the transition metals, and therefore, the edge position of the compounds has been determined to establish their formal oxidation state, the so called Kunzl's law.[44] In compounds with complex edges, it is not straightforward to determine the edge position. Therefore, fits were performed applying a Boltzmann sigmoidal function:[45]

$$(\text{norm. absorbance}) = \frac{A_1 - A_2}{1 + \exp\left(^{(E-E_0)}/_{E_d}\right)} \tag{1}$$

$E_0$ being the edge position, $E_d$ the curve slope at the edge, and $A_1$ and $A_2$ are the extremal *y* values of the sigmoidal (respectively 1 and 0 in the usual XAS normalization). The fitting parameters, including the edge positions, for the compounds studied and references are given in Table 2.

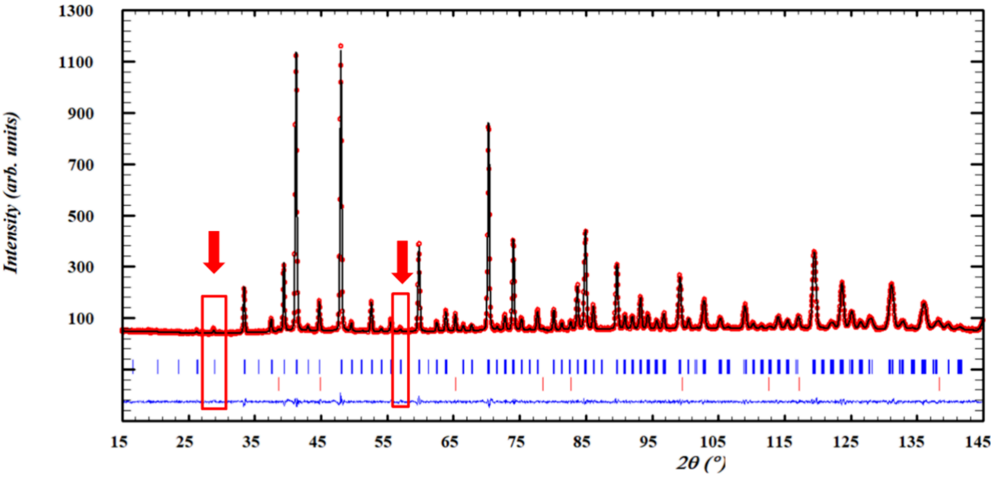

**Figure 6.** Graphic result of the fitting of NPD data of (LCSNT102000) with the model given in Table S1; experimental (red points), calculated (solid black line), and their difference (blue line at bottom) patterns are plotted. The vertical bars indicate the positions of the Bragg peaks of LCSNT102000 (upper row in blue) and NiO (lower row in red). Note the good fit of some ill-fitted peaks using S.G: *P*2$_1$/*n* reached by lowering the symmetry to S.G. *P*2$_1$ (indicated by the arrows in the figure).

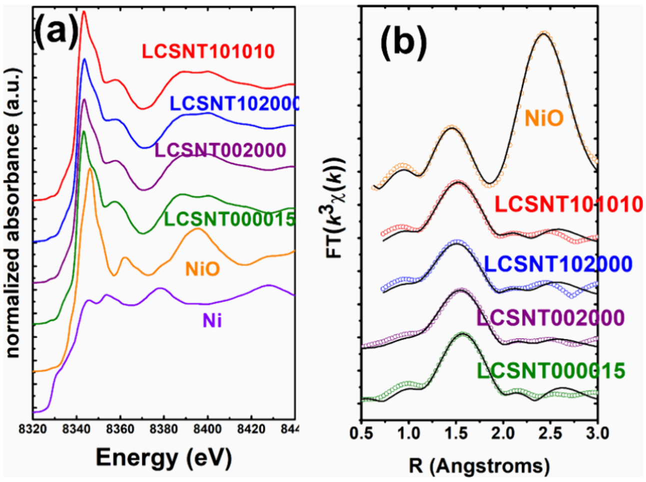

**Figure 7.** (a) XANES spectra of the Ni and NiO references and those of the studied compounds, and (b) fits of the EXAFS spectra in R space for the Ni local structure in the studied compounds.

Broadly speaking, for simple oxides, Kunzl's law is fulfilled as a good approximation. However, for complex oxides like the present ones, the transition-metal environment by itself may alter the electronic cloud, distorting the spectrum and resulting in false shifts. In any case, the law is still fulfilled but qualitatively, whereas other spectral features give information about the material. In this connection, in Figure 7a, the intensity of the main peak of the XANES spectrum decreases progressively in the sequence: LCSNT000015 > LCSNT101010 > LCSNT10200 = LCSNT002000. There are two plausible explanations for this:

i) That the Ni−O distances are increasing along the sequence. This can be ruled out based on the results from NPD presented in Table SI2: the distances between the 3d-metals and oxygen are larger in LCSNT101010 than in LCSNT102000, opposite to what expected from the XAS spectra.

ii) That the average coordination of the first-coordination sphere of Ni ions is decreasing. There is a clear correlation between the concentration of A-site vacancies and the intensity of the main peak: the bigger the former (it varies in the sequence: $\square_{0.15}$ (in LCSNT000015) > $\square_{0.10}$ (in LCSNT101010) > $\square_{0}$ (in LCSNT102000 and LCSNT002000), the more intense absorption. A possible explanation of this correlation would be based on the idea that A-site vacancies are defects formally charged negatively that may be associated with oxygen vacancies (formally charged positively) that in its turn may be concentrated on the B-site cations with lower oxidation state (nickel in the present materials instead of $Ti^{4+}$).

Thus, the nickel coordination spheres would be lower as the number of A-site vacancies increases. As a trend, this is what we observe (Table 3) from the fitting of the EXAFS, considering only the first Ni−O shell (Figure 7b) and considering the actual oxygen contents of the sample. So, LCSNT000015 and LCSNT002000 have the same oxygen content (Table 1) but the presence of A-site vacancies concentrates oxygen vacancies in the environment of nickel (Table 3); a similar situation is found when comparing LCSNT101010 and LCSNT102000. The reduction of the effective coordination number of nickel ions should result in a decrease of the absorption peak, but we found just the contrary. Thus, there are other influencing factors; understanding this point would require elaborate calculations that are beyond the scope of this work.

*Ti K-Edge.* Figure 8a shows the Ti K-edge spectra for the Ce-containing oxides LCSNT102000 and LCSNT101010; the edge position in both samples is the same energy corresponding to $Ti^{4+}$.[46] In Ti perovskites, the pre-edge of the Ti K-edge is highly sensitive to distortions in the Ti local environment.[46,47] The pre-edge region is usually subdivided into three or four main features (namely A, B, C, and D) as indicated in Figure 8b. The feature A has been attributed to 1s-3d ($e_g$) quadrupolar transitions and feature B to a mixture of 1s-3d($t_g$) quadrupolar and 1s−4p dipolar transitions when there is a fraction of 3d-4p orbital hybridization. The feature C has a dipolar character and is related to the interaction with neighboring Ti atoms (excitations from 1s to the $t_g/e_g$ levels of a neighbor $TiO_6$ octahedra). The intensity of the feature B is usually correlated to the off-center displacement of the Ti with respect to the octahedra (caused, for example, by thermal vibrations or distorted/incomplete $MO_n$ neighbor polyhedra).[46] The intensity and position of feature C have a strong dependence on the interactions between adjacent TiO6 octahedra. The spectra presented in Figure 8 show very weak A-features in both LCSNT101010 and LCSNT102000 compounds, but B and C are intense. In the former, both features B and C are more intense than in the latter, this being associated with more distorted and oxygen-deficient $MO_n$ polyhedra connected to the absorbing atom, in agreement with the existence of anionic vacancies in LCSNT101010 whereas in LCSNT102000, the oxygen substructure is complete.

**Magnetic Properties.** Figure 9 depicts the temperature dependence of the magnetic susceptibility per mole of nickel ($\chi$) obtained for the parent compound ($La_2NiTiO_6$ (LNT) with actual composition $La_2Ni_{0.964}Ti_{1.036}O_{6.00}$) and both derivatives (codoped with Sr and Ce (Table 4)). The former shows paramagnetic behavior above 100 K well described by a Curie−Weiss law $\chi_{CW} = \frac{C}{T-\theta}$ (where $C$ is the Curie constant and $\theta$ the Weiss temperature) plus a temperature-independent contribution $\chi_0$. The best fit of the data to this model (see Table 4 and Figure S6) yields a $C$ value that agrees with the theoretical one expected for a $Ni^{2+}$ ion in an octahedral environment, that is, taking into account the spin-only magnetic moment value and a

**Table 2. Summary of the Edge Fittings of the Studied Compounds and the Calculated Valences from the References**

| sample | $E_0$ (eV) | $E_d$ (eV) | $A_1$ | $A_2$ | $\Delta E$ (eV) | oxidation state |
|---|---|---|---|---|---|---|
| Ni | 8333.0 (2) | 4.3 (2) | 0.01 (2) | 1.00 (2) | 0 | 0 |
| NiO | 8335.3 (3) | 1.3 (2) | 0.02 (2) | 1.02 (2) | 2.3 | 2 |
| LCSNT000015 | 8335.8 (2) | 1.0 (2) | 0.02 (2) | 1.01 (2) | 2.8 | 2.4 (2) |
| LCSNT002000 | 8335.6 (2) | 1.0 (2) | 0.02 (2) | 1.01 (2) | 2.6 | 2.3 (2) |
| LCSNT102000 | 8335.8 (2) | 1.0 (2) | 0.02 (2) | 1.01 (2) | 2.8 | 2.4 (2) |
| LCSNT101010 | 8335.7 (2) | 1.0 (2) | 0.02 (2) | 1.02 (2) | 2.7 | 2.3 (2) |

Table 3. Summary of the Main EXAFS Parameters Obtained in the Fitting of the Spectra of the Studied Ni Compounds

| | $NiO_n$ shell | | | | |
|---|---|---|---|---|---|
| sample | $n/6$ | $\Delta R$ (A) | DW (A) | $E$ (eV) | $R$-factor |
| NiO reference | 0.99 ± 0.05 | 0.012 ± 0.001 | 0.0064 ± 0.0020 | −1 ± 1 | 0.005 |
| LCSNT000015 | 0.85 ± 0.15 | −0.022 ± 0.002 | 0.0038 ± 0.0009 | −3 ± 1 | 0.013 |
| LCSNT002000 | 0.92 ± 0.07 | −0.026 ± 0.002 | 0.0058 ± 0.0004 | −4.6 ± 0.8 | 0.005 |
| LCSNT102000 | 0.81 ± 0.08 | −0.083 ± 0.003 | 0.0066 ± 0.0011 | −3.5 ± 0.3 | 0.014 |
| LCSNT101010 | 0.76 ± 0.05 | −0.058 ± 0.003 | 0.0039 ± 0.0011 | −3 ± 1 | 0.012 |

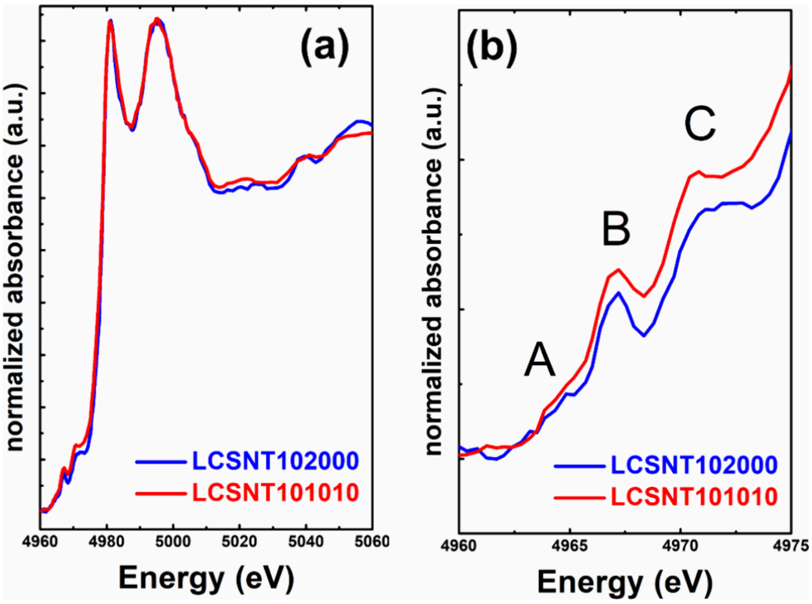

**Figure 8.** (a) XAFS at the Ti−K-edge of the LCSNT101010 and LCSNT102000 compounds; (b) detail of the pre-edge structure.

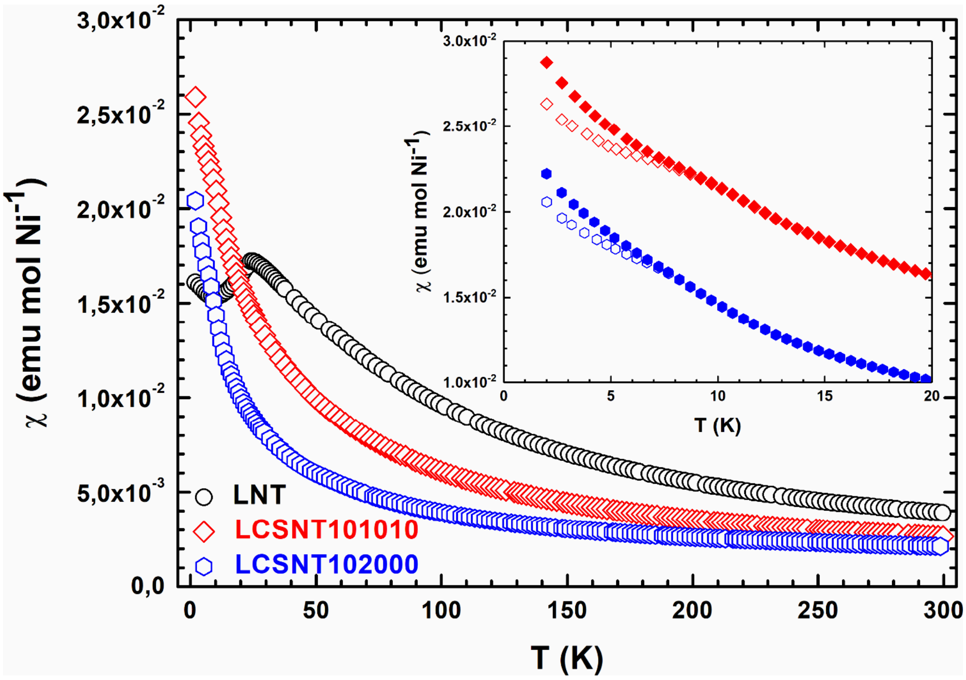

**Figure 9.** Magnetic susceptibility per mole of nickel as a function of temperature in an applied magnetic field of 100 mT of LNT (circles), LCSNT101010 (diamonds), and LCSNT102000 (hexagons). The inset shows the low-temperature data obtained for these two latter under zero-field-cooled (open symbols) and field-cooled (solid symbols) conditions.

partial contribution of the orbital magnetic moment, and the $\chi_0$ value agrees with the expected Van Vleck paramagnetism for such a cation, ∼100 × $10^{-6}$ emu $mol^{-1}$.[48,49] The negative value of $\theta$ corresponds to the antiferromagnetic interactions that give

Table 4. Relevant Data for Understanding the Magnetic Behavior of the Studied Compounds[a]

| compound | $\mu_{eff}$ ($\mu_B$/Ni) | $Ni^{n+}$ | $\mu_{theo}$ ($\mu_B$/Ni) | $Ni_{Ti}/Ni_{Ni}$ (%) | $\chi = \frac{C}{T - \theta} + \chi_0$ | $T_N$ (K) |
|---|---|---|---|---|---|---|
| **LNT** | 3.06 | 2.00(2) | 3.23 | 7.6(3)/88.8(3) | $\frac{1.21(1)}{T + 27.3(9)} + 2.1(2) \times 10^{-4}$ | 24.8 |
| **LCSNT101010** | 2.54 | 2.00(9) | 3.23 | 31.4(4)/59.8(4) | does not follow the Curie−Weiss Law | |
| **LCSNT102000** | 2.23 | 2.1(1) | 3.07 | 49(1)/49(1)[b] | does not follow the Curie−Weiss Law | |
| **LCSNT000015** | 3.02 | 2.0(2) | 3.23 | 5.4(2)/81.6(4) | $\frac{1.18(1)}{T + 28.8(9)} + 2.4(2) \times 10^{-4}$ | 23.4 |

[a] Chemical composition obtained from neutron and X-ray powder diffraction data. Experimental effective magnetic moment ($\mu_{eff}$) calculated as $\sqrt{8\chi T}$ at room temperature, where $\chi$ is the experimental magnetic susceptibility expressed per mole of nickel. The oxidation state of nickel ($Ni^{n+}$) was determined according to the chemical composition. Expected magnetic moment ($\mu_{theor}$) calculated considering $\mu = 3.23\ \mu_B$ for $Ni^{2+}$[48] and $\mu = 1.86\ \mu_B$ for low-spin $Ni^{3+}$.[51] Percentage of the B-site of the titanium (B″ position) occupied by nickel ($Ni_{Ti}$) and percentage of the B-site of the nickel (B′ position) occupied by nickel ($Ni_{Ni}$), considering a rock-salt order between both elements. Result of the best fit of the experimental $\chi$ data to the Curie-Weiss law plus a temperature-independent contribution ($\chi_0$). Néel temperature ($T_N$). [b] These values denote a random distribution.

rise to the long-range magnetic order developed below 24.8 K, according to the well-defined maximum observed in the magnetic susceptibility ($\frac{\partial\chi(T)}{\partial T} = 0$) at that temperature. Below 10 K, $\chi$ increases as the temperature decreases rather than tending to a value close to two-thirds of the $\chi$ value at the maximum ($1.15 \times 10^{-2}$ emu mol $Ni^{1-}$) as predicted by the mean field theory for antiferromagnetism.[49] All this is in accordance with the previously reported magnetic behavior.[32,50]

The two derivative compounds LCSNT101010 and LCSNT102000 show $\chi$ values lower than those of the starting compound down to 20 and 10 K, respectively. This is evident in the values of the effective magnetic moment ($\mu_{eff}$) obtained at room temperature, which are shown in Table 4. While the $\mu_{eff}$ value for the parent oxide (3.06 $\mu_B$) is close to the expected value for $Ni^{2+}$ with a $^3A_{2g}$ ground term (3.23 $\mu_B$), the values for the LCSNT101010 (2.54 $\mu_B$) and LCSNT102000 (2.23 $\mu_B$) oxides are considerably lower than those expected ($\mu_{theo}$) for the mixed valence scenario described above (see Table 4). Furthermore, the variation of $\chi$ with temperature for both compounds is hardly compatible with a Curie−Weiss law, even including a temperature-independent term, as indicated by the nonlinear dependence of $\chi^{-1}$ with $T$, shown in Figure S6. This deviation from a straight line is most pronounced for the LCSNT102000 compound, whose $\mu_{eff}$ also shows the largest deviation from the expected value.

On the other hand, a sharp contrast at low temperature is observed between the magnetic behavior of the parent compound and its derivatives, since for these latter ones, there is no evidence of long-range magnetic order and just rather faint changes of slope appear below 10 K, a significantly low temperature. In addition, below the temperatures at which the bumps appear, there is divergence between the magnetic susceptibilities ZFC and FC; see inset in Figure 9, and both increase as temperature decreases. AC magnetic susceptibility measurements rule out the existence of a spin-glass-like state. The low-temperature magnetic behavior ($T < 20$ K) of both derivative compounds appears quite similar, although the compound LCSNT101010 shows a more evident change of slope and a larger divergence than the LCSNT102000 compound. There is also similarity in the dependence of the magnetization with the applied magnetic field obtained at 50, 15, and 2 K, although the compound LCSNT101010 presents higher magnetization values than the compound LCSNT102000. As can be seen in Figure 10, at 50 K, the magnetization shows a linear dependence on the applied magnetic field, while at 15 and 2 K, a downward deviation from linearity is observed at high fields. The deviation at 2 K is greater than at 15 K. Magnetic hysteresis is apparent at 2 K in both compounds (see Figure S7), but not at 15 K. Hysteresis loops show remanent magnetization values of $1.4 \times 10^{-3}\ \mu_B$/Ni and $7.1 \times 10^{-4}\ \mu_B$/Ni for LCSNT101010 and LCSNT102000 compounds, respectively. Such similarities suggest that neither the existence of $Ni^{3+}$ nor the presence of oxygen vacancies (see Table 4) plays a crucial role in the observed magnetic properties of both compounds.

In the monoclinic parent compound, the magnetic order of the face-centered nickel sublattice is determined by Ni−O−Ti−O−Ni superexchange magnetic interactions, which take place between nearest neighbors (nn) and between next nearest neighbors (nnn), these latter interactions being the stronger.[50,52−54] Thus, we have focused our attention on the nickel sublattice to try to understand the observed magnetic behavior in the two monoclinic derivative oxides. Specifically, we consider the observed deviation from the ideal nickel sublattice occupation, which consists of titanium overstoichiometry (see compositions in Table 4) and occupation of the titanium sublattice by nickel atoms. This antisite defect is quantified by the $Ni_{Ti}$ parameter (see Table 4), whose value for an ideal ordered occupation is 0%.

Overstoichiometry of titanium has been reported previously for the parent compound and derivatives with nominal compositions $La_{2-x}Sr_xNiTiO_{6-\delta}$ ($0 \leq x \leq 0.5$)[32] and $La_{2-x}NiTiO_{6-\delta}$ ($0 \leq x < 0.2$).[27] Of all of them, LSCNT000015 shows a high titanium overstoichiometry, and its magnetic behavior is practically identical to that of the parent compound, though with a lower Néel temperature (see Table 4). It should be noted that this compound shows a quite low amount of $Ni^{3+}$ (0.7%) as well as a low number of antisites, in a similar way to the starting compound (see Table 4). It is also worth noting that a compound with an even higher titanium overstoichiometry ($La_{1.92(4)}Ni_{0.81(3)}Ti_{1.19(3)}O_{6.00}$) was synthesized for this same series,[27] and that it exhibits a Néel temperature of 20.6 K (Figure S8). Therefore, the Néel temperature decreased from 24.8 to 20.6 K; as observed with the increase of titanium overstoichiometry from 0.036 to 0.19 can be understood as a dilution effect on the Ni−O−Ti−O−Ni superexchange magnetic interactions. Consequently, titanium overstoichiometry is not the cause of the significantly different magnetic behavior observed in the two derivatives, LCSNT101010 and LCSNT102000, compared to the parent compound.

https://doi.org/10.1021/acs.jpcc.5c05743
J. Phys. Chem. C 2025, 129, 21183−21196

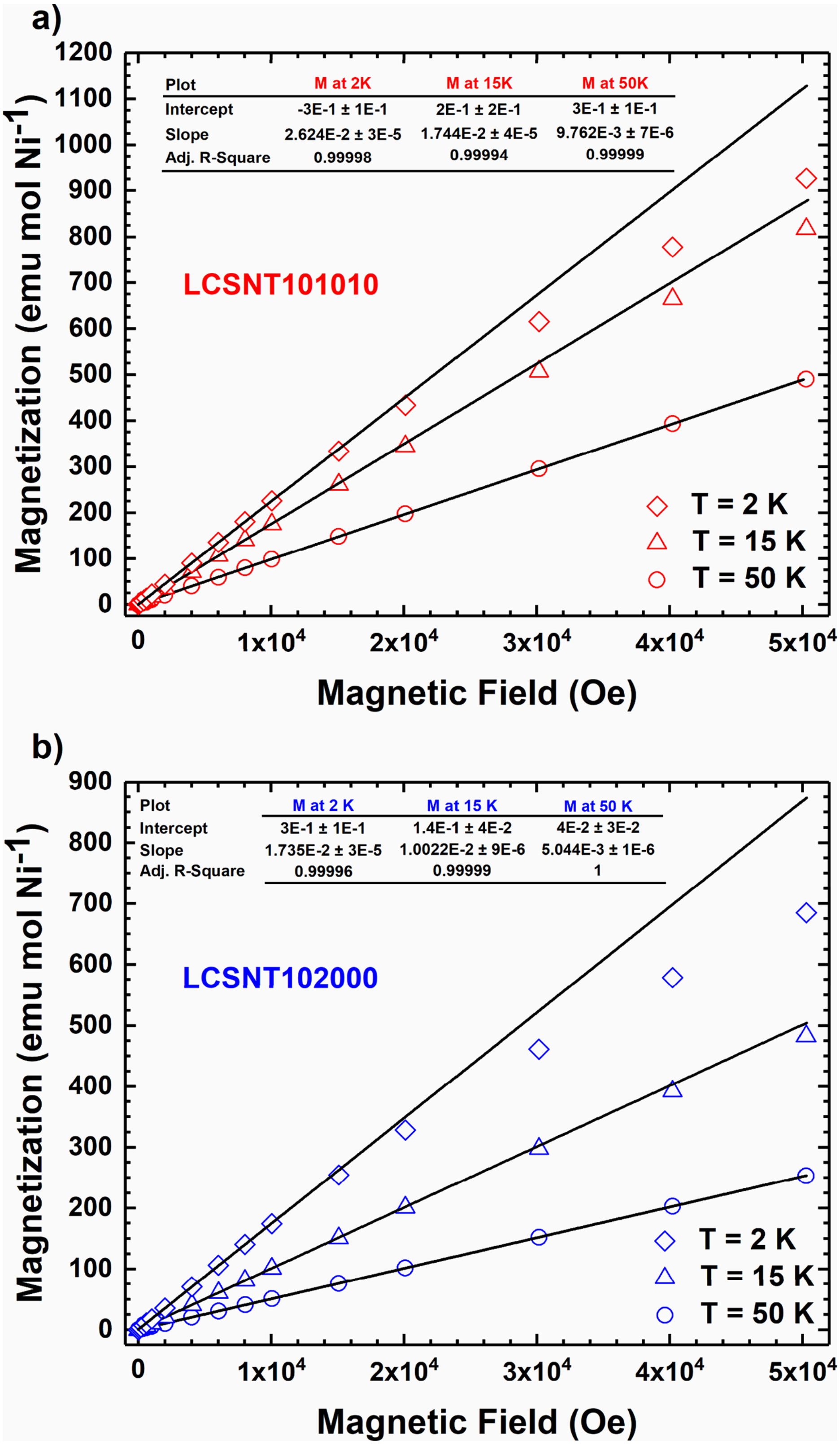

| Plot | M at 2K | M at 15K | M at 50K |
|---|---|---|---|
| Intercept | -3E-1 ± 1E-1 | 2E-1 ± 2E-1 | 3E-1 ± 1E-1 |
| Slope | 2.624E-2 ± 3E-5 | 1.744E-2 ± 4E-5 | 9.762E-3 ± 7E-6 |
| Adj. R-Square | 0.99998 | 0.99994 | 0.99999 |

| Plot | M at 2 K | M at 15 K | M at 50 K |
|---|---|---|---|
| Intercept | 3E-1 ± 1E-1 | 1.4E-1 ± 4E-2 | 4E-2 ± 3E-2 |
| Slope | 1.735E-2 ± 3E-5 | 1.0022E-2 ± 9E-6 | 5.044E-3 ± 1E-6 |
| Adj. R-Square | 0.99996 | 0.99999 | 1 |

**Figure 10.** Magnetic field dependence of the virgin magnetization of (a) LCSNT101010) and (b) LCSNT102000 derivative compounds, measured at 2 K (diamonds), 15 K (triangles), and 50 K (circles). Black lines are the fitted linear functions, whose parameters are displayed in the table along with the linear fit statistics. For $T$ = 50 K, the linear fits were made over the entire range of the applied magnetic field, while for $T$ = 2 and 15 K, they were limited to values between 0 and 10 kOe, both inclusive.

Regarding the occupation of the titanium sublattice by nickel, as can be seen in Table 4, the compound LCSNT101010 (with lanthanum vacancies) presents a large number of antisites ($Ni_{Ti}$ = 31.4 ± 0.4%), although a high degree of short-range ordering at B-sites persists as indicated by NPD data, while for the derived compound LCSNT102000 (without lanthanum vacancies), the

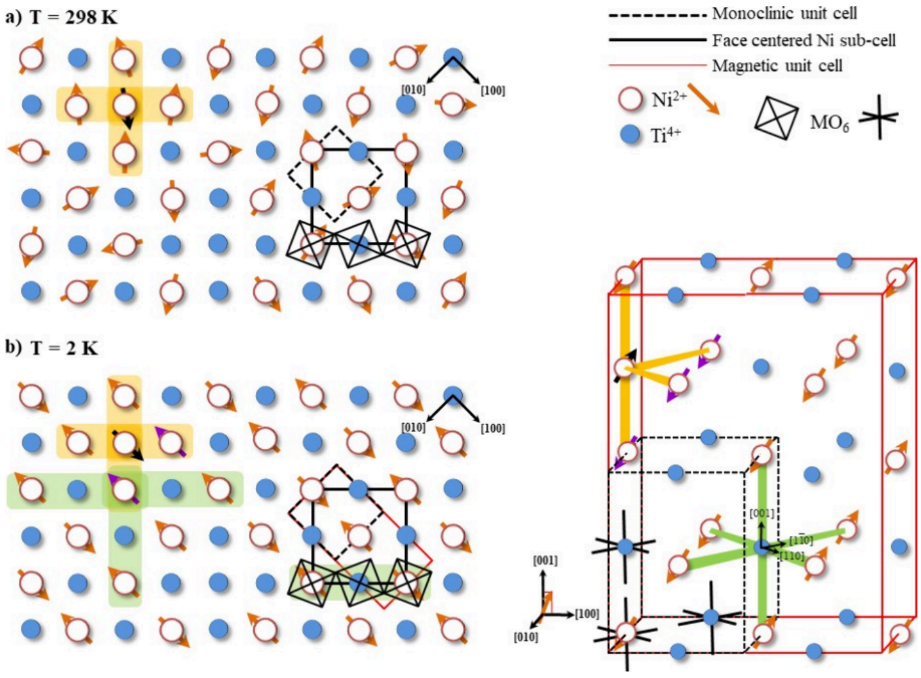

**Figure 11.** Schematic illustrations of ordered distribution of Ni$^{2+}$ (empty circle) and Ti$^{4+}$ (full circle) ions of the idealized crystal structure of the La$_2$NiTiO$_6$ compound, where just one Ni$^{2+}$(Ti$^{4+}$) ion occupies the B-position of the Ti$^{4+}$(Ni$^{2+}$). Oxide and lanthanum ions are omitted for simplicity. The arrows represent the magnetic moments of Ni$^{2+}$ ions, differentiating by black color that of the Ni$^{2+}$ ion that forms the antisite defect. Ni$^{2+}$−O−Ti$^{4+}$−O−Ni$^{2+}$ nnn interaction paths are highlighted in green and Ni$^{2+}$−O−Ni$^{2+}$ interaction paths in orange. (a) View of the plane (001) with $z = 0$ in the paramagnetic state ($T > T_N$) where antiferromagnetic correlations take place between the nickel antisite and its four immediate nickel neighbors (six in three-dimensional space) due to the Ni$^{2+}$−O−Ni$^{2+}$ superexchange interactions. (b) Antiferromagnetic state ($T < T_N$) consisting of a type II magnetic structure[50] governed by Ni$^{2+}$−O−Ti$^{4+}$−O−Ni$^{2+}$ nnn superexchange interactions. On the left, a view of the plane (001) with $z = 0$, and to the right, the magnetic unit cell with propagation vector $\mathbf{k} = [1/2,0,1/2]$. The six magnetic moments immediately around the magnetic moment of the antisite cannot fulfill simultaneously the Ni$^{2+}$−O−Ni$^{2+}$ and Ni$^{2+}$−O−Ti$^{4+}$−O−Ni$^{2+}$ nnn superexchange interactions (this is highlighted in the plane (001) for one of them by the overlap of the green and orange rounded rectangles). The drawn configuration of these seven magnetic moments, as an example within the numerous possible configurations, corresponds to the minor disruption of the antiferromagnetic structure caused by the predominance of the first type of superexchange interaction. Thus, three magnetic moments (purple) of the six, one for each interaction path, have an inverse orientation to that expected according to the type II magnetic structure.

value of the Ni$_{Ti}$ parameter (49 ± 1%) corresponds to a random distribution of the nickel and titanium atoms but without evidence from NPD of short-range order. Therefore, the suppression of the long-range antiferromagnetic order in these two derivatives lies in the existence of an insufficient structural order between nickel and titanium that avoids exceeding a percolation threshold value for interconnectivity between Ni atoms of the Ni−O−Ti−O−Ni type. Moreover, antisite defects allow for the presence of neighboring nickel atoms closer than in the ideal ordered distribution, so that new magnetic interactions may be established between them. These are Ni−O−Ni superexchange interactions, antiferromagnetic in nature like the mentioned above nnn interactions, but which can be much stronger, as indicated by the high Néel temperatures of the compounds that exhibit them, such as NiO (523 K)[55] and perovskite-type PbNiO$_3$ (225 K).[56]

This scenario of coexistence of the superexchange magnetic interactions Ni$^{2+}$−O−Ti$^{4+}$−O-Ni$^{2+}$ and Ni$^{2+}$−O-Ni$^{2+}$ is depicted in Figure 11, where paramagnetic and antiferromagnetic states of the starting compound are considered. In the paramagnetic state ($T > 50$ K) (see Figure 11a), the nickel atom that forms the antisite defect develops a strong antiferromagnetic correlation to the six nickel atoms immediately surrounding it, and the response of these seven magnetic moments to an external magnetic field will be lower than the response experienced by the rest of magnetic moments. Thus, at a given temperature, the higher the number of antisites, the lower the magnetic susceptibility. This is clearly observed in Figure 9 and in the calculated values of $\mu_{\mathrm{eff}}$ shown in Table 4. Furthermore, two different contributions to the magnetic susceptibility may be considered, one from the magnetic moments unrelated to Ni−O−Ni interactions and another from the magnetic moments involved in such interactions. The first one will follow a Curie−Weiss law according to the antiferromagnetic interactions mentioned above, while the second one will not due to the intensification of the antiferromagnetic correlation as the temperature decreases. In the case of the starting compound, with a Ni$_{Ti}$ parameter value of 7.6%, the first contribution type predominates, while for the two derived compounds, with a Ni$_{Ti}$ parameter value greater than 30%, the second contribution type is important enough to cause deviation from Curie−Weiss behavior (see Figure S6) in such a way that the greater the number of antisites, the greater the deviation. Therefore, it is possible to justify the paramagnetic behavior observed in the three compounds based on the number of antisites.

When the temperature is low enough, the long-range order of nickel magnetic moments involved in Ni−O−Ti−O−Ni interactions takes place, generating a type II antiferromagnetic structure[50] by the prevalence of superexchange interactions along crystallographic directions [110], [1$\bar{1}$0], and [001] (see Figure 11b). In reality, the three superexchange paths are virtually identical ($d_{Ni-Ni}$ ~8.01 Å and bond angle $Ni^{2+}-O-Ti^{4+}$ ~156 °).[32] However, the six neighboring magnetic moments closest to the nickel atom that forms the antisite defect are also involved in Ni−O−Ni interactions, which take place in the same three crystallographic directions with interaction paths likely very similar to each other. Thus, it is impossible for all six moments to satisfy both interactions at the same time (see Figure 11b). The orientation of these seven moments is subject to conjecture, but it is evident that whatever the configuration of moments adopted, this type of cluster will suppose the local disruption of the antiferromagnetic order as well as the appearance of a small local net magnetic moment. This moment may be responsible for the observed increase in $\chi$ below 10 K in the starting compound and, in fact, in all members of the $La_{2-x}NiTiO_{6-\delta}$ series,[27] since the low values of the $Ni_{Ti}$ parameter that they present (less than 8%) likely allow the existence of such clusters well isolated from each other within an antiferromagnetic matrix.

The low-temperature scenario is quite different for the two derivative compounds since the value of the $Ni_{Ti}$ parameter is much higher, resulting in a microstructure change that excludes long-range antiferromagnetism, as mentioned above. Despite this high degree of disorder at B-sites, the derived compound LCSNT101010 presents short-range order (Figure 3), whereas in the derived compound LCSNT102000, that short-range order does not exist over regions widespread enough to be detected by powder neutron diffraction (Figure 6). This may be a result of the role played by lanthanum vacancies as promoters of the ordered distribution of Ni and Ti atoms at B-sites.[27] Considering all this and taking into account that both derivatives show similar magnetic behaviors at low temperature, we hypothesize that antisite defects experience a clustering high enough to allow the existence of relatively large clusters of nickel atoms. These clusters are surrounded by a matrix with nickel and titanium atoms partially ordered at a short range because their Ti/Ni ratio is high. For compound LCSNT102000, the Ti/Ni ratio is high enough to generate a matrix where the short-range order is more spatially limited and hence not detectable by neutron diffraction. From the magnetic point of view, we consider that the magnetic moments of the matrix undergo magnetic interactions Ni−O−Ti−O−Ni, resulting in a short-range antiferromagnetic order or an antiferromagnetic correlation depending on the number of neighboring magnetic moments. As for clusters, the magnetic moments located inside are governed by the antiferromagnetic interactions Ni−O−Ni, while those located in the periphery can acquire their own orientation under the influence of the interactions with the magnetic moments of the matrix and the applied magnetic field. This could be the origin of the maximum bump and irreversibility observed below 10 K.

## ■ CONCLUSIONS

Obtaining single-phase samples by substituting $La^{3+}$ simultaneously by the pair $Ce^{4+}/Sr^{2+}$ in the starting compounds $La_{2-p}Vac_pNiTiO_6$ (with $p = 0$ and 0.1) is only achieved up to a $Ce^{4+}$ content of 0.1 per formula unit. Two new materials with compositions $La_{1.60(1)}Ce_{0.10(1)}Sr_{0.30(1)}Ni_{0.98(2)}Ti_{1.02(2)}O_{6.00(1)}$ ($p = 0$, LCSNT102000) and $La_{1.60(1)}Ce_{0.10(1)}Sr_{0.20(1)}Ni_{0.91(2)}Ti_{1.09(2)}O_{5.89(4)}$ ($p = 0.1$, LCSNT101010) have been obtained. The combined use of complementary characterization techniques (SR-HRPD, NPD, HREM, and XAS) allows concluding that both compounds present a perovskite-like structure of monoclinic symmetry, with the same octahedra tilting scheme ($a^-a^-c^+$) with a high percentage of antisite defects accompanied by some Ti overstoichiometry; thus, $Ti^{4+}$ ions occupy $Ni^{2+}$ positions to some extent. The antisite percentage is 31% for LCSNT101010, which allows the existence of short-range order; on the contrary, for LCSNT102000, it is as high as 49%, generating a complete disorder. The adoption of an average monoclinic structure is attributed to the presence of three distinct cationic species randomly distributed at the A position; besides, in LCSNT101010, A-site vacancies exist. To accommodate this complex situation, an oxygen substructure with sufficient degrees of freedom is needed to generate up to six distinct first-coordination spheres around position A (occupied by $La^{3+}$, $Ce^{4+}$, and $Sr^{2+}$ and, in some cases, cation vacancies) and position B (occupied by $Ni^{2+}$ and $Ti^{4+}$). In LCSNT102000, additional ordering of the A-cations is produced, lowering the symmetry from $P2_1/n$ in LCSNT101010 to $P2_1$.

The two compounds derived by codoping exhibit a more complex magnetic behavior than the long-range antiferromagnetic order that appears in the starting compound. There are also differences between the two derivatives, albeit they are more subtle. Their magnetic behaviors are linked to the occupation degree of the titanium sublattice by nickel atoms. These antisite defects generate a structural disorder between nickel and titanium high enough to avoid reaching a percolation threshold value for interconnectivity between Ni atoms of the Ni−O−Ti−O−Ni type, giving rise to the suppression of long-range antiferromagnetic order. These antisite defects also allow the onset of strong superexchange antiferromagnetic Ni−O−Ni interactions, giving rise to magnetic susceptibility values lower than those observed for the starting compound at a given temperature above $T_N$. This results in a decrease in the effective magnetic moment of $Ni^{2+}$ at room temperature of 17% for LCSNT101010 and 27% for LCSNT102000 compared to that observed for LNT. We propose that superexchange Ni−O−Ti−O-Ni and Ni−O−Ni antiferromagnetic interactions exist in all three compounds, so that in LNT, the low number of antisite defects allows them to be isolated from each other and, therefore, almost all of the magnetic moments of $Ni^{2+}$ are involved in the Ni−O−Ti−O−Ni interactions. In LCSNT101010, the number of antisite defects allows their clustering and the consequent formation of a matrix with a high Ti/Ni ratio in which large clusters are embedded. Thus, Ni−O−Ni interactions are confined within clusters, short-range Ni−O−Ti−O-Ni interactions will occur in the matrix, and finally, the magnetic moments of $Ni^{2+}$ located at the periphery of the clusters will be simultaneously involved in both types of interactions. In LCSNT102000, the increased number of antisite defects increases the number of Ni−O−Ni interactions at the expense of decreasing the number of Ni−O−Ti−O-Ni interactions in the matrix and thus decreasing the number of $Ni^{2+}$ magnetic moments involved in both types of interactions.

## ■ ASSOCIATED CONTENT

### Supporting Information

The Supporting Information is available free of charge at https://pubs.acs.org/doi/10.1021/acs.jpcc.5c05743.

XRD patterns for LCSNT102000 and LCSNT101010, BSE and NPD for LCSNT200020, schematic representation of the structure of LCSNT102000, reciprocal magnetic susceptibility for LCSNT101010 and LCSNT102000 (PDF)

## AUTHOR INFORMATION

### Corresponding Authors

**M. Teresa Azcondo** − *CEU Universities, Facultad de Farmacia, Departamento de Química y Bioquímica, Urbanización Montepríncipe, Universidad San Pablo-CEU, Boadilla del Monte, Madrid E-28668, Spain;* orcid.org/0000-0002-3890-0800; Email: azcondo@ceu.es

**Ulises Amador** − *CEU Universities, Facultad de Farmacia, Departamento de Química y Bioquímica, Urbanización Montepríncipe, Universidad San Pablo-CEU, Boadilla del Monte, Madrid E-28668, Spain;* orcid.org/0000-0002-4412-2419; Email: uamador@ceu.es; Fax: (34) 91 351 04 96

### Authors

**Mercedes Yuste** − *CEU Universities, Facultad de Farmacia, Departamento de Química y Bioquímica, Urbanización Montepríncipe, Universidad San Pablo-CEU, Boadilla del Monte, Madrid E-28668, Spain*

**Alejandro Gómez-Pérez** − *CEU Universities, Facultad de Farmacia, Departamento de Química y Bioquímica, Urbanización Montepríncipe, Universidad San Pablo-CEU, Boadilla del Monte, Madrid E-28668, Spain*

**Clemens Ritter** − *Institut Laue-Langevin, Grenoble Cedex 9 38042, France;* orcid.org/0000-0003-3674-3378

**Álvaro Muñoz Noval** − *Departamento de Física de Materiales, Facultad de Físicas, Universidad Complutense, Madrid E-28040, Spain; SpLine Spanish CRG Beamline, ESRF, Grenoble 38042, France;* orcid.org/0000-0003-3236-5509

**Julio Romero de Paz** − *Unidad de Magnetometría y Criogenia del CAI Técnicas Físicas, Facultad de Ciencias Físicas de la Universidad Complutense de Madrid, Ciudad Universitaria, Madrid 28040, Spain; Departamento de Ingeniería Química Industrial y del Medio Ambiente, Escuela Técnica Superior de Ingenieros Industriales de la Universidad Politécnica de Madrid, Madrid 28006, Spain*

**Khalid Boulahya** − *Departamento de Química Inorgánica, Facultad Ciencias Químicas, Univ. Complutense, Madrid E-28040, Spain;* orcid.org/0000-0001-9912-5329

**Flaviano García-Alvarado** − *CEU Universities, Facultad de Farmacia, Departamento de Química y Bioquímica, Urbanización Montepríncipe, Universidad San Pablo-CEU, Boadilla del Monte, Madrid E-28668, Spain;* orcid.org/0000-0002-5698-2598

Complete contact information is available at:
https://pubs.acs.org/10.1021/acs.jpcc.5c05743

### Author Contributions

The authors contributed equally.

### Notes

The authors declare no competing financial interest.

## ACKNOWLEDGMENTS

The results of this article are part of the projects PID2022-139501OB-C21, PID2022-139501OB-C22, and PID2022-139039OB-C21, funded by MCIN/AEI/10.13039/501100011033/FEDER,UE. This research has been also supported by the "Plan de Recuperación, Transformación y Resiliencia-C17.I1", with funds from the European Union-Next Generation EU, "European Regional Development Fund" as part of the action after the COVID-19 pandemic, and Comunidad de Madrid for the project "(GREEN H2-CM)". We also thank ILL for financial support and for beam time allocation: experiment codes 5-22-720, doi:10.5291/ILL-DATA.5-22-720, and 5-23-646, doi:10.5291/ILL-DATA.5-23-646, and CSIC for financial support and ESRF (SpLine, BM25 line) for beam time allocation for experiment 25-01-933. M.T.A., M.Y., A.G.P., F.G.-A., and U.A. also thank Universidad San P-CEU for the financial support.

## REFERENCES

(1) Mitchell, R. H. *Perovskite: Modern and Ancient*; Almaz Press: Ontario, Canada, 2002.

(2) Adler, S. B. Factors Governing Oxygen Reduction in Solid Oxide Fuel Cell Cathodes. *Chem. Rev.* **2004**, *104*, 4791−4844.

(3) Liu, Z.; Han, M.-F.; Miao, W.-T. Preparation and characterization of graded cathode $La_{0.6}Sr_{0.4}Co_{0.2}Fe_{0.8}O_{3-\delta}$. *J. Power Sources* **2007**, *173*, 837−841.

(4) Sun, X.; Wang, S.; Wang, Z.; Qian, J.; Wen, T.; Huang, F. Evaluation of $Sr_{0.88}Y_{0.08}TiO_3-CeO_2$ as composite anode for solid oxide fuel cells running on $CH_4$ fuel. *J. Power Sources* **2009**, *187*, 85−89.

(5) Skinner, S. J. Recent advances in Perovskite-type materials for solid oxide fuel cell cathodes. *Int. J. Inorg. Mater.* **2001**, 3, 113−121.

(6) Hrovat, M.; Katsarakis, N.; Reichmann, K.; Bernik, S.; Kuščer, D.; Holc, J. Characterisation of LaNi1 − xCoxO3 as a possible SOFC cathode material. *Solid State Ion.* **1996**, *83*, 99−105.

(7) Drennan, J.; Tavares, C. P.; Steele, B. C. H. An electron microscope investigation of phases in the system La−Ni−O. *Mater. Res. Bull.* **1982**, *17*, 621−626.

(8) Zinkevich, M.; Aldinger, F. Thermodynamic analysis of the ternary La−Ni−O system. *J. Alloys Compd.* **2004**, *375*, 147−161.

(9) Chiba, R.; Yoshimura, F.; Sakurai, Y. An investigation of $LaNi_{1-x}Fe_xO_3$ as a cathode material for solid oxide fuel cells. *Solid State Ion.* **1999**, *124*, 281−288.

(10) Knudsen, J.; Friehling, P. B.; Bonanos, N. Effect of A-site stoichiometry on phase stability and electrical conductivity of the perovskite $La_s(Ni_{0.59}Fe_{0.41})O_{3-\delta}$ and its compatibility with $(La_{0.85}Sr_{0.15})_{0.91}MnO_{3-\delta}$ and $Zr_{0.85}Y_{0.15}O_{2.925}$. *Solid State Ion.* **2005**, *176*, 1563−1569.

(11) Konysheva, E.; Irvine, J. T. S. In Situ High-Temperature Neutron Diffraction Study of A-Site Deficient Perovskites with Transition Metals on the B-Sublattice and Structure−Conductivity Correlation. *Chem. Mater.* **2011**, *23*, 1841−1850.

(12) Konysheva, E. Y.; Xu, X.; Irvine, J. T. S. On the Existence of A-Site Deficiency in Perovskites and Its Relation to the Electrochemical Performance. *Adv. Mater.* **2012**, *24*, 528−532.

(13) Tao, S.; Irvine, J. T. S. A redox-stable efficient anode for solid-oxide fuel cells. *Nat. Mater.* **2003**, *2*, 320−323.

(14) Yakovlev, S. O.; Kharton, V. V.; Naumovich, E. N.; Zekonyte, J.; Zaporojtchenko, V.; Kovalevsky, A. V.; Yaremchenko, A. A.; Frade, J. R. Defect formation and transport in $La_{0.95}Ni_{0.5}Ti_{0.5}O_{3-\delta}$. *Solid State Sci.* **2006**, *8*, 1302−1311.

(15) Bian, L.; Duan, C.; Wang, L.; O'Hayre, R.; Cheng, J.; Chou, K.-C. Ce-doped $La_{0.7}Sr_{0.3}Fe_{0.9}Ni_{0.1}O_{3-\delta}$ as symmetrical electrodes for high performance direct hydrocarbon solid oxide fuel cells. *J. Mater. Chem. A* **2017**, *5*, 15253−15259.

(16) Chen, M.; Zhang, H.; Yao, C.; Lou, H.; Zhang, Z.; Xia, B.; Sun, Y.; Wang, X.; Lang, X.; Cai, K. Ce-doping enhanced ORR kinetics and $CO_2$ tolerance of $Nd_{1-x}Ce_xBaCoFeO_{5+\delta}$ (x = 0−0.2) cathodes for solid oxide fuel cells. *Ceram. Int.* **2024**, *50*, 18416−18425.

(17) Choi, H.; Fuller, A.; Davis, J.; Wielgus, C.; Ozkan, U. S. Ce-doped strontium cobalt ferrite perovskites as cathode catalysts for solid oxide fuel cells: Effect of dopant concentration. *Appl. Catal. B: Environ.* **2012**, *127*, 336−341.

(18) Guo, R.; Liu, X.; Li, X.; Xue, Y.; Gao, Y.; Jin, F.; Tian, Y.; Ling, Y. Enhancing the $CO_2$ electrolysis performance by Ce doped $La_{0.7}Sr_{0.3}Fe_{0.9}Ni_{0.1}O_{3-\delta}$ electrode in symmetric solid oxide electrolysis cell. *Int. J. Hydrogen Energy* **2024**, *78*, 1142−1148.

(19) Li, S.; Liu, Y.; Cai, C.; Xue, K.; Bian, L.; An, S. Ce-doped promotes the phase stability and electrochemical performance of $SrCoO_{3-\delta}$ cathode for intermediate-temperature solid oxide fuel cells. *J. Power Sources* **2024**, *592*, No. 233932.

(20) Yang, Q.; Wu, H.; Song, K.; Beshiwork, B. A.; Luo, X.; Tian, D.; Zhu, S.; Lu, X.; Ding, Y.; Chen, Y.; Lin, B. Tuning $Ba_{0.5}Sr_{0.5}Co_{0.8}Fe_{0.2}O_{3-\delta}$ cathode to high stability and activity via Ce-doping for ceramic fuel cells. *Ceram. Int.* **2022**, *48*, 31418−31427.

(21) de Irujo-Labalde, X. M.; Goto, M.; Urones-Garrote, E.; Amador, U.; Ritter, C.; Amano-Patino, M.; Shimakawa, Y.; García-Martín, S. Charge Evolution in the $Y_{0.9}Ba_{1.7}Ca_{2.4}Fe_5O_{14.7}$ Layered Perovskite. *Chem. Mater.* **2024**, *36*, 5184−5191.

(22) Martínez de Irujo-Labalde, X.; Goto, M.; Urones-Garrote, E.; Amador, U.; Ritter, C.; Amano Patino, M. E.; Koedtruad, A.; Tan, Z.; Shimakawa, Y.; García-Martín, S. Multiferroism Induced by Spontaneous Structural Ordering in Antiferromagnetic Iron Perovskites. *Chem. Mater.* **2019**, *31*, 5993−6000.

(23) Azcondo, M. T.; Orfila, M.; Marugán, J.; Sanz, R.; Muñoz-Noval, A.; Salas-Colera, E.; Ritter, C.; García-Alvarado, F.; Amador, U. Novel Perovskite Materials for Thermal Water Splitting at Moderate Temperature. *ChemSusChem* **2019**, *12*, 4029−4037.

(24) Azcondo, M. T.; Romero de Paz, J.; Boulahya, K.; Ritter, C.; García-Alvarado, F.; Amador, U. Complex magnetic behaviour of $Sr_2CoNb_{1-x}Ti_xO_6$ ($0 \leq x \leq 0.5$) as a result of a flexible microstructure. *Dalton Trans.* **2015**, *44*, 3801−3810.

(25) de Irujo-Labalde, X. M.; Amador, U.; Ritter, C.; Goto, M.; Patino, M. A.; Shimakawa, Y.; García-Martín, S. 3D to 2D Magnetic Ordering of $Fe^{3+}$ Oxides Induced by Their Layered Perovskite Structure. *Inorg. Chem.* **2021**, *60*, 8027−8034.

(26) Maupoey, Z.; Azcondo, M. T.; Amador, U.; Kuhn, A.; Pérez-Flores, J. C.; Romero de Paz, J.; Bonanos, N.; García-Alvarado, F. The role of the $Eu^{3+}/Eu^{2+}$ redox-pair in the electrical properties of $Sr_2EuNb_{1-x}Ti_xO_{6-\delta}$ oxides. *J. Mater. Chem.* **2012**, *22*, 18033−18042.

(27) Pérez-Flores, J. C.; Pérez-Coll, D.; García-Martín, S.; Ritter, C.; Mather, G. C.; Canales-Vázquez, J.; Gálvez-Sánchez, M.; García-Alvarado, F.; Amador, U. A- and B-Site Ordering in the A-Cation-Deficient Perovskite Series $La_{2-x}NiTiO_{6-\delta}$ ($0 \leq x < 0.20$) and Evaluation as Potential Cathodes for Solid Oxide Fuel Cells. *Chem. Mater.* **2013**, *25*, 2484−2494.

(28) Yuste, M.; Pérez-Flores, J. C.; de Paz, J. R.; Azcondo, M. T.; García-Alvarado, F.; Amador, U. New perovskite materials of the $La_{2-x}Sr_xCoTiO_6$ series. *Dalton Trans.* **2011**, *40*, 7908−7915.

(29) Fracchia, M.; Coduri, M.; Ghigna, P.; Anselmi-Tamburini, U. Phase stability of high entropy oxides: A critical review. *J. Eur. Ceram. Soc.* **2024**, *44*, 585−594.

(30) Tang, L.; Li, Z.; Chen, K.; Li, C.; Zhang, X.; An, L. High-entropy oxides based on valence combinations: design and practice. *J. Am. Ceram. Soc.* **2021**, *104*, 1953−1958.

(31) Rosendo, P.; Azcondo, M. T.; Biancotto, L.; Anemone, G.; Boulahya, K.; Ritter, C.; Amador, U. Defects and Defect Association Determine the Actual Entropy of Perovskites Derived from Lanthanum−Calcium Ferrite. *Inorg. Chem.* **2025**, *64*, 12446−12457.

(32) Perez Flores, J. C.; Ritter, C.; Perez-Coll, D.; Mather, G. C.; Garcia-Alvarado, F.; Amador, U. Synthesis, structures and electrical transport properties of the $La_{2-x}Sr_xNiTiO_{6-\delta}$ ($0 \leq x \leq 0.5$) perovskite series. *J. Mater. Chem.* **2011**, *21*, 13195−13204.

(33) Kakihana, M.; Tada, M.; Shiro, M.; Petrykin, V.; Osada, M.; Nakamura, Y. Structure and Stability of Water Soluble $(NH_4)_8[Ti_4(C_6H_4O_7)_4(O_2)_4]\cdot 8H_2O$. *Inorg. Chem.* **2001**, *40*, 891−894.

(34) Rubio-Zuazo, J.; Collado-Negro, V.; Heyman, C.; Ferrer, P.; da Silva, I.; Gallastegui, J. A.; Gutiérrez-León, A.; Castro, G. R. A double crystal X-ray monochromator for the SpLine diffraction and absorption synchrotron bending magnet beamline at the ESRF. *J. Phys.: Conf. Ser.* **2013**, *425*, No. 052005.

(35) Rodríguez-Carvajal, J. Recent advances in magnetic structure determination by neutron powder diffraction. *Physica B: Condensed Matter* **1993**, *192*, 55−69.

(36) Ravel, B.; Newville, M. ATHENA, ARTEMIS, HEPHAESTUS: data analysis for X-ray absorption spectroscopy using IFEFFIT. *J. Synchrotron Radiat.* **2005**, *12*, 537−541.

(37) Ankudinov, A. L.; Ravel, B.; Rehr, J. J.; Conradson, S. D. Real-space multiple-scattering calculation and interpretation of x-ray-absorption near-edge structure. *Phys. Rev. B* **1998**, *58*, 7565−7576.

(38) Pomjakushin, V. On the magnetic and crystal structures of NiO and MnO. *Acta Crystallogr.* **2024**, *B80*, 385−392.

(39) Choi, H.; Fuller, A.; Davis, J.; Wielgus, C.; Ozkan, U. S. Ce-doped strontium cobalt ferrite perovskites as cathode catalysts for solid oxide fuel cells: Effect of dopant concentration. *Appl. Catal., B* **2012**, *127*, 336−341.

(40) Glazer, A. The classification of tilted octahedra in perovskites. *Acta Crystallogr.* **1972**, *B28*, 3384−3392.

(41) King, G.; Woodward, P. M. Cation ordering in perovskites. *J. Mater. Chem.* **2010**, *20*, 5785−5796.

(42) Gómez-Pérez, A.; Azcondo, M. T.; Yuste, M.; Pérez-Flores, J. C.; Bonanos, N.; Porcher, F.; Muñoz-Noval, A.; Hoelzel, M.; García-Alvarado, F.; Amador, U. The A-cation deficient perovskite series $La_{2-x}CoTiO_{6-\delta}$ ($0 \leq x \leq 0.20$): new components for potential SOFC composite cathodes. *J. Mater. Chem. A* **2016**, *4*, 3386−3397.

(43) Yang, J. H.; Choo, W. K.; Lee, J. H.; Lee, C. H. The crystal structure of the B-site ordered complex perovskite $Sr(Yb_{0.5}Nb_{0.5})O_3$. *Acta Crystallogr.* **1999**, *B55*, 348−354.

(44) Kunzl, V. A linear dependence of energy levels on the valency of elements. *Collect. Czech. Chem. Commun.* **1932**, *4*, 213−224.

(45) Sowrey, F. E.; Skipper, L. J.; Pickup, D. M.; Drake, K. O.; Lin, Z.; Smith, M. E.; Newport, R. J. Systematic empirical analysis of calcium−oxygen coordination environment by calcium K-edge XANES. *Phys. Chem. Chem. Phys.* **2004**, *6*, 188−192.

(46) Vedrinskii, R. V.; Kraizman, V. L.; Novakovich, A. A.; Demekhin, Ph. V.; Urazhdin, S. V. Pre-edge fine structure of the 3d atom K x-ray absorption spectra and quantitative atomic structure determinations for ferroelectric perovskite structure crystals. *J. Phys.: Condens.* **1998**, *10*, 9561.

(47) Itié, J. P.; Couzinet, B.; Dhaussy, A. C.; Flank, N.; Jaouen, A. M.; Lagarde, P.; Polian, A. X-ray absorption spectroscopy on titanate perovskites at the Ti K edge. *High Pressure Res.* **2006**, *26*, 325−330.

(48) Figgis, B. N.; Hitchman, M. A. *Ligand Field Theory and Its Applications*; Special Topics In Inorganic Chemistry: Wiley India, 2010.

(49) Mabbs, F. E.; Machin, D. J. *Magnetism and Transition Metal Complexes*; Dover Books on Chemistry; Dover Publications Inc.: New York, USA, 2008.

(50) Rodríguez, E.; López, M. L.; Campo, J.; Veiga, M. L.; Pico, C. Crystal and magnetic structure of the perovskites $La_2MTiO_6$ (M = Co, Ni). *J. Mater. Chem.* **2002**, *12*, 2798−2802.

(51) Ganguly, P.; Demazeau, G.; Dance, J. M.; Hagenmuller, P. An ESR investigation of the electronic localization on nickel (III) in perovskite-type rare-earth-nickel oxides. *Solid State Commun.* **1990**, *73*, 617−622.

(52) Seehra, M. S.; Giebultowicz, T. M. Magnetic structures of fcc systems with nearest-neighbor and next-nearest-neighbor exchange interactions. *Phys. Rev. B* **1988**, *38*, 11898−11900.

(53) Philipp, J. B.; Majewski, P.; Reisinger, D.; Geprägs, S.; Opel, M.; Erb, A.; Alff, L.; Gross, R. Magnetoresistance and Magnetic Properties of the Double Perovskites. *Acta Phys. Polym., A* **2004**, *105*, 7−16.

(54) Karolak, M.; Edelmann, M.; Sangiovanni, G. Nickel-titanium double perovskite: A three-dimensional spin-1 Heisenberg antiferromagnet. *Phys. Rev. B* **2015**, *91*, No. 075108.

(55) Srinivasan, G.; Seehra, M. S. Magnetic susceptibilities, their temperature variation, and exchange constants of NiO. *Phys. Rev. B* **1984**, *29*, 6295−6298.

(56) Inaguma, Y.; Tanaka, K.; Tsuchiya, T.; Mori, D.; Katsumata, T.; Ohba, T.; Hiraki, K.-i.; Takahashi, T.; Saitoh, H. Synthesis, Structural Transformation, Thermal Stability, Valence State, and Magnetic and Electronic Properties of $PbNiO_3$ with Perovskite- and $LiNbO_3$-Type Structures. *J. Am. Chem. Soc.* **2011**, *133*, 16920−16929.